PAPER

Check for updates

Redox-active oxide-molten salt composites as a new family of high-capacity thermal energy storage materials†

Hilal Bektas, [ID] [a] Runxia Cai, [ID] ‡[a] Saqlain Raza,[b] Jun Liu[b] and Fanxing Li [ID] *[a]

This study introduces a new family of redox-active oxide-molten salt (ROMS) composites for high-capacity thermal energy storage. Porous perovskite oxides serve as active support materials, facilitating thermochemical energy storage through redox reactions, while latent heat from the phase change of the salt mixture enables high energy density within a narrow temperature swing. We demonstrated the compatibility between perovskites and salt mixtures, with 12 out of 25 tested combinations proving successful. The diverse properties of perovskites and salt mixtures resulted in ROMS compositions with different functionality and performance, three of which are highlighted in this work. $La_{0.8}Sr_{0.2}FeO_{3-\delta}$:NaF−CaF$_2$−LiF exhibited excellent latent heat-based energy storage as well as long-term stability with a total capacity of $\sim$530 kJ kg^{-1} (510−660 °C). $Sr_{0.125}Ca_{0.875}Fe_{0.25}Mn_{0.75}O_{3-\delta}$:NaF−CaF$_2$ achieved the overall energy density of $\sim$523 kJ kg^{-1} (670−820 °C) through both phase-transition and redox-based mechanisms, though gradual deactivation was observed over long-term operation. Lastly, $La_{0.8}Sr_{0.2}FeO_{3-\delta}$:Li$_2MoO_4$, a highly redox-active ROMS composition, delivered up to 875 kJ kg^{-1} when applied for waste heat recovery from fuel-containing exhaust gas streams.

1. Introduction

The combustion of fossil fuels, which accounts for approximately 80% of the world's energy utilization, stands as the predominant contributor to greenhouse gas emissions.[1–3] Meanwhile, only less than half of the energy derived from fossil fuels is converted into useful forms such as electric power, with the rest being discharged as waste heat.[4] Other energy-intensive industries such as iron and steelmaking also produce vast amounts of high-grade heat (>500 °C), with processes like electric arc furnaces or coke ovens generating exhaust gas at high temperatures.[5,6] As such, capturing the excess heat for industrial applications or power generation would significantly improve the energy efficiency of the processes and substantially reduce the carbon emissions.[4,5,7] However, the recovery of waste heat faces challenges due to the mismatch between the operational requirements of energy supply and demand.[4] Also, the intermittency or fluctuations of many heat sources restrict the continuous operation of the waste heat recovery system.[8,9]

Thermal energy storage (TES) can overcome these challenges by adapting to the properties of high-temperature heat sources.[10–12] A cost-effective thermal energy storage system can capture the energy from the heat source, and store and release it on demand for industrial processes or power generation.[12,13]

TES can find applications in the forms of sensible, latent, and thermochemical heat. Among these, sensible heat storage materials have been most widely investigated and commercially mature owing to their simplicity.[13,14] Molten nitrate salts are the most commonly used sensible heat storage materials for medium (200–400 °C) to high (>400 °C) temperature TES, often employed as heat transfer fluids due to their favorable characteristics such as high heat capacity and low melting point.[15,16] For example, $LiNO_3$−$NaNO_3$−KNO_3−$Ca(NO_3)_2$, extensively studied for sensible heat storage application, has been utilized as heat transfer fluid in solar parabolic systems.[11,17,18] Nitrate salts can provide energy storage densities ranging from 100 to 500 kJ kg^{-1} but they require large temperature swings of $\sim$300 °C to achieve the high values.[13,19,20] In addition, the relatively low decomposition temperatures of molten nitrate salts limit their applicability for temperatures exceeding 560 °C.[13]

Compared to sensible heat storage materials, latent heat storage systems that rely on phase change materials (PCM) exhibit notable advantages, primarily due to their superior energy storage density, which requires low volume and operates within a narrow temperature range.[11,12] For medium- and high-temperature (200–1400 °C) applications, fluoride, and carbonate-type molten salts are particularly attractive phase-

[a]*Department of Chemical and Biomolecular Engineering, North Carolina State University, 911 Partners Way, Raleigh, North Carolina 27695, USA. E-mail: fli5@ncsu.edu*

[b]*Department of Mechanical and Aerospace Engineering, North Carolina State University, Raleigh, North Carolina 27695, USA*

† Electronic supplementary information (ESI) available. See DOI: https://doi.org/10.1039/d5ta02329g

‡ Present address: School of Mechanical Engineering, Shanghai Jiao Tong University, 800 Dongchuan RD, Minhang District, Shanghai, China.

change materials (PCM) for latent heat storage with their considerably large heat of fusion.[21] They are suitable for use at operating temperatures above 500 °C due to their high melting points. However, the application of molten salts is restricted by thermal instabilities above the melting point. Besides, the melting and solidification of PCMs cause handling difficulties in fluidized beds or single-tank systems. The corrosive nature of molten salts imposes additional limitations on their applications in heat storage.[13,22]

To address the above-mentioned challenges, there has been growing interest in form-stable composite materials consisting of PCMs and supporting materials in recent years.[10,11,23–27] Form-stable composite materials enclose the PCMs within a skeleton material and reduce the leakage of PCMs.[24] Various supporting materials, such as diatomite,[25,28,29] vermiculite,[26] magnesium oxide,[23] and expanded graphite,[30] have been used to fabricate the composite materials. Among them, diatomite has attracted more interest owing to its high porosity, corrosion resistance, and low cost.[10,25] For example, Jiang et al. used a porous modified diatomite-based skeleton material to improve the thermophysical properties of NaNO$_3$.[25] They obtained a total energy storage density of 382.92 kJ kg^{-1} in the operating temperature range of 130–330 °C with 58.67 wt% salt loading and improved the micro-flow of molten salt within the large pores of the modified diatomite. Li et al. studied sodium nitrate-expanded vermiculite (EV) composite materials, achieving a latent heat of 157.2 kJ kg^{-1}, and a high salt : EV ratio of 734.6 wt% (defined as adsorptive capacity) using the direct impregnation method.[26] Jiang et al. developed a form-stable composite material using LiNO$_3$–NaNO$_3$–KNO$_3$–Ca(NO$_3$)$_2$ and calcium silicate with a melting point of 103.5 °C and latent heat of 73.59 kJ kg^{-1}.[11] The high porosity of calcium silicate played a vital role in preventing salt leakage by absorbing large amounts of nitrate salt, thus ensuring the long-term stability of over 1000 thermal cycles. While these studies have mainly focused on low (<200 °C) and medium temperatures (200–400 °C) applications due to the low melting point of nitrate salts, efforts have been made to extend the operating temperature range to high temperatures (>400 °C). Qian et al., for instance, introduced a group of composite materials consisting of polyethylene glycol, LiNO$_3$, and Na$_2$SO$_4$ which were aimed to be used in low, middle, and high-temperature energy storage, respectively.[24] Furthermore, Ge et al. also proposed a composite material for the medium and high temperature ranges, by using LiCO$_3$–NaCO$_3$ as the PCM, MgO as the ceramic support material, and additionally carbon nanotubes as the thermal conductivity enhancer.[23] Their studies emphasized the significance of good wettability of the salt with ceramic material to ensure the formation of a robust composite material. Although the proposed composite materials offer promising properties and prevent salt leakage, inert support materials limit the energy efficiency of such composites, necessitating a large temperature swing for effective heat storage.

Alternatively, thermochemical energy storage (TCES) has recently gained significant attention owing to its potential for achieving high energy density in wide operating temperature ranges and extended durations.[19,31] Particularly, TCES systems, which utilize the chemical energy of reversible redox reactions of metal oxides, have been widely studied in recent years.[32,33] Within the realm of redox-active metal oxide materials, perovskite oxides with the general formula of ABO$_3$ (where A is typically an alkali, alkaline earth, or a lanthanide metal cation and B is a transition metal cation) have shown considerable advantages over conventional redox materials.[34,35] They have the ability to continuously exchange their lattice oxygen over a wide range of temperatures and partial oxygen pressures, facilitating thermochemical energy storage under flexible operating conditions.[36,37] Conversely, the redox reactions of monometallic oxides are discrete and restricted to specific high temperatures.[32] Furthermore, the flexible structures of perovskite oxides enable tailorable thermochemical properties, allowing them to be utilized in various energy storage applications.[38] The excellent kinetics of perovskites, attributed to their high lattice oxygen diffusion rate, further enhances their utility.[33,39] To date, perovskite oxides have demonstrated TCES densities ranging from 34 to 571 kJ kg^{-1}-ABO$_3$ with an operating temperature window extending up to 1250 °C.[34–47] However, they require large temperature and oxygen partial pressure swings to achieve such densities, thereby limiting the energetic efficiency of the processes.

To address the limitations of existing TES materials, this study reports a new class of materials, i.e. redox-active oxide-molten salt (ROMS) composites, which combine molten salts and perovskite oxides in a dual-phase composite structure.[48] In these composites, the latent heat storage from the phase change of molten salts serves as the primary energy storage mechanism, while redox-active oxide materials act as supporting structures to prevent salt leakage and contribute additional thermochemical energy density through redox reactions. ROMS composites offer several potential advantages: (1) the oxide exoskeleton stabilizes the molten salt via favorable surface tensions, similar to non-redox-active composites;[27] (2) the latent heat storage of molten salts narrows the temperature swing required for redox-based energy storage; (3) both perovskite oxides and molten salts are highly tunable, enabling compatibility with a range of operating conditions; and (4) the high redox activity facilitates efficient recovery of waste heat from fuel-containing exhaust streams. This study demonstrates the compatibility of perovskite oxides and salt mixtures as energy storage media, highlighting three compositions with varying features that cater to different application scenarios ranging from thermal energy only to high-temperature fuel containing flue gas.

2. Experimental methods

2.1 Material preparation

The abbreviations and synthesis methods of metal oxides that were used are listed in Table 1. LSF1 and LSFCo were commercial La$_{0.8}$Sr$_{0.2}$Fe$_{0.97}$O$_{3-\delta}$ and La$_{0.8}$Sr$_{0.2}$Co$_{0.8}$Fe$_{0.2}$O$_{3-\delta}$, respectively obtained from Praxair Surface Technologies while the rest was synthesized either by solid-state or sol–gel method. Detailed descriptions regarding the solid-state method can be found in our previous study.[49] The procedure for the sol–gel

This journal is © The Royal Society of Chemistry 2025

J. Mater. Chem. A, 2025, **13**, 20028–20043 | **20029**

Table 1 The abbreviation of metal oxides that were used in composite materials

Sample name	Abbreviation	Synthesis method
$Ca_2AlMnO_{5+\delta}$	CAM	Sol–gel
$SrFeO_{3-\delta}$	SF	Ball mill
$Sr_{0.75}Ba_{0.25}FeO_{3-\delta}$	SBF	Ball mill
$Sr_{0.25}Ca_{0.75}Fe_{0.25}Mn_{0.75}O_{3-\delta}$	SCFM1	Sol–gel
$Sr_{0.125}Ca_{0.875}Fe_{0.25}Mn_{0.75}O_{3-\delta}$	SCFM2	Sol–gel
$Sr_{0.05}Ca_{0.95}Mn_{0.95}Co_{0.05}O_{3-\delta}$	SCMCo1	Ball mill
$Sr_{0.05}Ca_{0.95}Mn_{0.9}Co_{0.1}O_{3-\delta}$	SCMCo2	Ball mill
$La_{0.8}Sr_{0.2}FeO_{3-\delta}$	LSF1	Commercial
$La_{0.6}Sr_{0.4}FeO_{3-\delta}$	LSF2	Ball mill
$La_{0.7}Sr_{0.3}FeO_{3-\delta}$	LSF3	Ball mill
$La_{0.3}Sr_{0.7}Co_{0.9}Mn_{0.1}O_{3-\delta}$	LSCoM1	Ball mill
$La_{0.7}Sr_{0.3}Co_{0.9}Mn_{0.1}O_{3-\delta}$	LSCoM2	Ball mill
$La_{0.8}Sr_{0.2}Co_{0.8}Fe_{0.2}O_{3-\delta}$	LSFCo	Commercial

method is provided in the ESI.† Eutectic and ternary salt mixtures were prepared by mixing the salts in a mortar with the specific ratios provided in Table 2. The salts used in this study were LiF (97%), NaF (99%), CaF_2 (99%), MgF_2 (99%), and KF (99%), from Thermo Fisher Scientific and Li_2CO_3 (≥99%), Na_2CO_3 (≥99.5%) NaCl (≥99.5%), and Li_2MoO_4 (99.9%) from Sigma Aldrich. The composite materials were prepared by using facile mixing and sintering, as illustrated in Fig. 1b. Fig. 1b is adopted to prepare the composites using either as received oxides or the porous oxides prepared *via* Fig. 1a. Detailed descriptions regarding material preparation for XRD, TGA-DSC tests as well as preparation of pellets for thermal conductivity measurements can be found in the ESI.†

For the long-term tests, we applied the salt-grinding method to the perovskite oxides to obtain a porous structure before preparing the composite material. Schematic representation of this method is provided in Fig. 1a. The perovskite oxides were mixed with NaCl and 3 mm ZrO_2 beads in a stainless-steel sample jar with a specific mass ratio. The jar was ball milled at 1200 rpm for 24 h using a high-energy ball mill. The resulting mixtures were rinsed with distilled water to remove NaCl using the centrifuge tube for 8 min at 6000 rpm. This rinsing step was repeated 3 times. Afterward, the remaining wet particles were

dried in a vacuum oven at 80 °C for 30 min and then at 130 °C overnight. BET surface area, pore width, and volume of LSF1 were determined using a Micromeritics ASAP 2020 instrument. First, the samples were degassed at 200 °C for 10 hours to get rid of the adsorbed species on the surface. After that, nitrogen adsorption isotherms were obtained in the relative pressure range (P/P^0) of 0.01–1 at 77 K.

2.2 Characterization

We characterized the crystal structures of the composite materials using an Empyrean PANalytical XRD with Cu-Kα radiation ($\lambda = 1.5406$ Å) at an operating voltage of 45 kV and a current of 40 mA. XRD patterns were collected over a 2θ range of 15° to 80°, with a step size of 0.0262° holding for 0.4 s for each step. Additionally, LSF1:LiF–NaF–CaF_2 (post-100 cycles) was scanned using a high-temperature stage XRK900 since the spent sample was more prone to absorb moisture. The sample was ramped up to 200 °C in an N_2 atmosphere to remove hydrates. Phase analysis was performed using *HighScore* software. We examined the surface morphologies of LSF1 and LSF1:LiF–NaF–CaF_2 using a Hitachi SU8700 field-emission scanning electron microscope (FESEM) coupled with energy-dispersive X-ray spectroscopy (EDS).

2.3 TGA-DSC and thermal conductivity measurements

We determined melting/crystallization enthalpy and temperature by means of a differential scanning calorimeter (DSC with ±2% accuracy) coupled with a thermogravimetric analyzer (TGA, TA-Instrument, SDT Q650). The heat flow was calibrated using a sapphire reference with a known heat capacity. Prior to each experiment, cell constant calibration was verified using aluminum wire to obtain a calibration constant, which was then used to correct the measured heat of fusion. In each experiment, we placed 10–13 mg of YSZ (yttria-stabilized zirconia) as inert material and then 10–15 mg of the sample into a 110 μm platinum (Pt) pan. Inert material was necessary to prevent the salt from sticking to the Pt pan upon melting.[52] For the composite materials containing NaF–CaF_2, an additional ~30 mg of YSZ was placed on top to diminish the thermal losses. To minimize potential inaccuracies caused by the

Table 2 The ratios and phase change properties of eutectic salts reported in the literature

Salt mixture	Weight ratio	Heat of fusion (kJ kg_{salt}^{-1})	Melting point (°C)
Li_2CO_3–Na_2CO_3 [50]	0.44–0.56	370	496
LiF–NaF–CaF_2 [51]	0.35–0.38–0.26	640	615
NaF–CaF_2 [52,53]	0.53–0.47	520–600	810
MgF_2–NaF–CaF_2 [52,53]	0.14–0.52–0.34	510–540	745–754
NaF–NaCl [54]	0.26–0.73	572	674
NaF–KF [53]	0.33–0.67	550–560	721
LiF–CaF_2 [53]	0.54–0.46	750–760	766
LiF–NaF [51,55]	0.49–0.51	816[a]	649
Li_2MoO_4 [56]	—	280	705

[a] The eutectic point for LiF–NaF was provided with a mole ratio of 0.61–0.39 in the FactSage database, heat of fusion was reported for a ratio of 0.6–0.4 in Phillips *et al.*'s study.[51]

20030 | *J. Mater. Chem. A*, 2025, **13**, 20028–20043
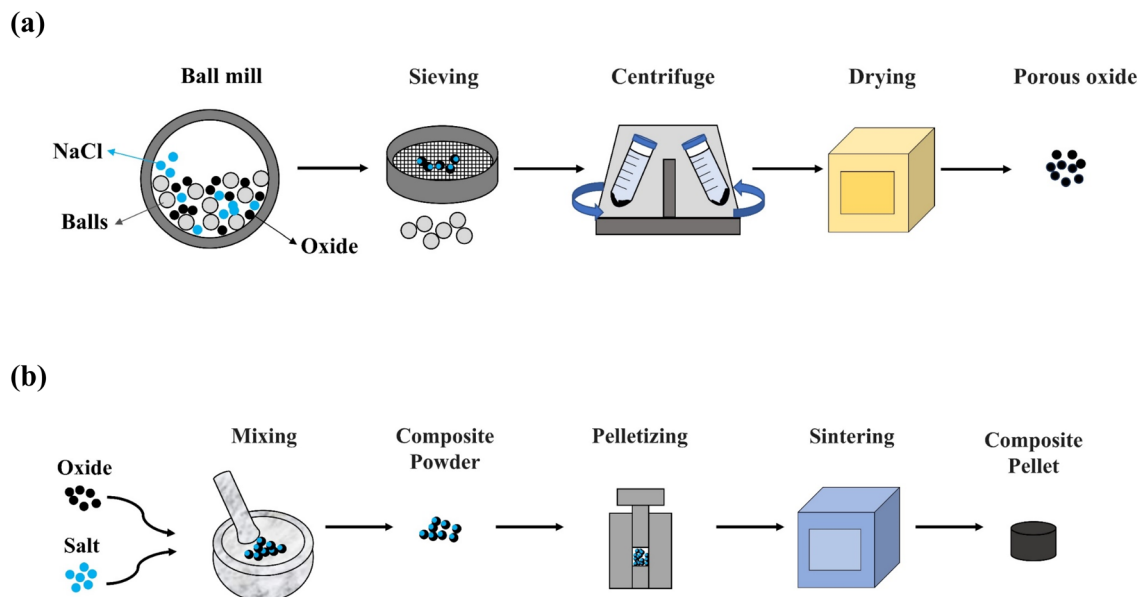
This journal is © The Royal Society of Chemistry 2025

Fig. 1 Schematic representation of material preparation (a) salt-grinding method for the formation of porous oxide (b) composite material preparation *small portion of the composite particles were used for TGA-DSC tests, while the rest was prepared for the XRD analysis.*

deflection of heat from shiny Pt pans, we used an alumina lid on top, resulting in more consistent measurements. The experiments were conducted over a temperature range of 150 °C, determined based on the melting/solidification point of the salt used in the ROMS (*e.g.*, 670–820 °C for SCFM2:NaF–CaF$_2$). First, the samples were heated up to 180 °C to remove the absorbed moisture, and the weight at the end of this step was used as the initial weight. The samples were then cycled between the lower and upper temperature limits at a ramping rate of 10 °C min^{-1}, with 15 min isothermal steps. Typically, the first two cycles were carried out in an Ar atmosphere at a total gas flow rate of 200 ml min^{-1}, followed by alternating between 20% O$_2$/80% Ar at the upper temperature and Ar at the lower temperature. For the experiments under reducing conditions, samples were first ramped up to 730 °C under Ar and then exposed to 20% H$_2$/80% Ar until equilibrium was reached. After that, the samples were ramped down to 580 °C under Ar, followed by exposure to 20% O$_2$/80% Ar. Details regarding TGA-DSC analysis and calculation of overall energy density are described in the ESI.†

We measured the thermal conductivities of LSF1, LiF–NaF–CaF$_2$, and the composite material LSF1:LiF–NaF–CaF$_2$ *via* the transient plane source technique using the Hot Disc sensor, which is a widely accepted approach for determining thermal properties of materials.[57–59] Details regarding this method can be found in the ESI.†

3. Results and discussion

3.1 Compatibility between perovskite oxides and eutectic salt mixtures

The compatibility between various metal oxides and eutectic salt mixtures was first evaluated using XRD. The formation of new phases other than the target oxide and salt phases would indicate a reaction between the oxides and the salts. This is undesirable as it degrades the energy capacity of the sample, as demonstrated by the measured melting enthalpies of SF:LiF–NaF and SBF:LiF–NaF, detailed in Table S2† (exact compositions of metal oxides can be found in Table 1). Overall, 12 out of 25 samples screened were compatible. The XRD patterns of the compatible samples were presented in Fig. 2 and 3 and the identified crystal phases for all the samples were summarized in Table 3. In general, the Ca- and Ba-based oxides were less likely to react with NaF, CaF$_2$, and NaCl. However, when LiF or MgF$_2$ were introduced in the salt mixtures, the B-site cation(s) of the perovskite oxides tended to form new oxide phases with the cations of fluoride salts. Additionally, cations of SBF and SF led to the formation of new fluorides by breaking the eutectic phase of the salt mixture. Some of the resulting fluoride phases, such as SrF$_2$ or KCaF$_3$, can be associated with their relatively higher stability compared to initial fluoride phases, as shown in Table S1† based on data from the Materials Project database.[60] Although the relative stability of fluorides based on the Materials Project database offers a useful guide, it cannot explain all the formed phases, since it does not consider the potential favorability of competing mixed oxide phases; the benefits and limitations of this approach are further discussed in ESI.†

On the other hand, La-based oxides were revealed to be more stable as they showed less tendency to react with salt mixtures in general. Our results suggested that increasing Sr in the A-site reduced the stability of the oxide structure. The higher stability of perovskite oxides with rare earth metals compared to alkaline earth metals was also supported by Jacobs *et al.*'s study through convex hull analysis.[61] Thus, lower Sr in the A-site ensured a compatible composite structure with LiF–NaF–CaF$_2$ and MgF$_2$–NaF–CaF$_2$. This phenomenon was observed for LSCM2 and LSCM1; the former formed a compatible composite

This journal is © The Royal Society of Chemistry 2025

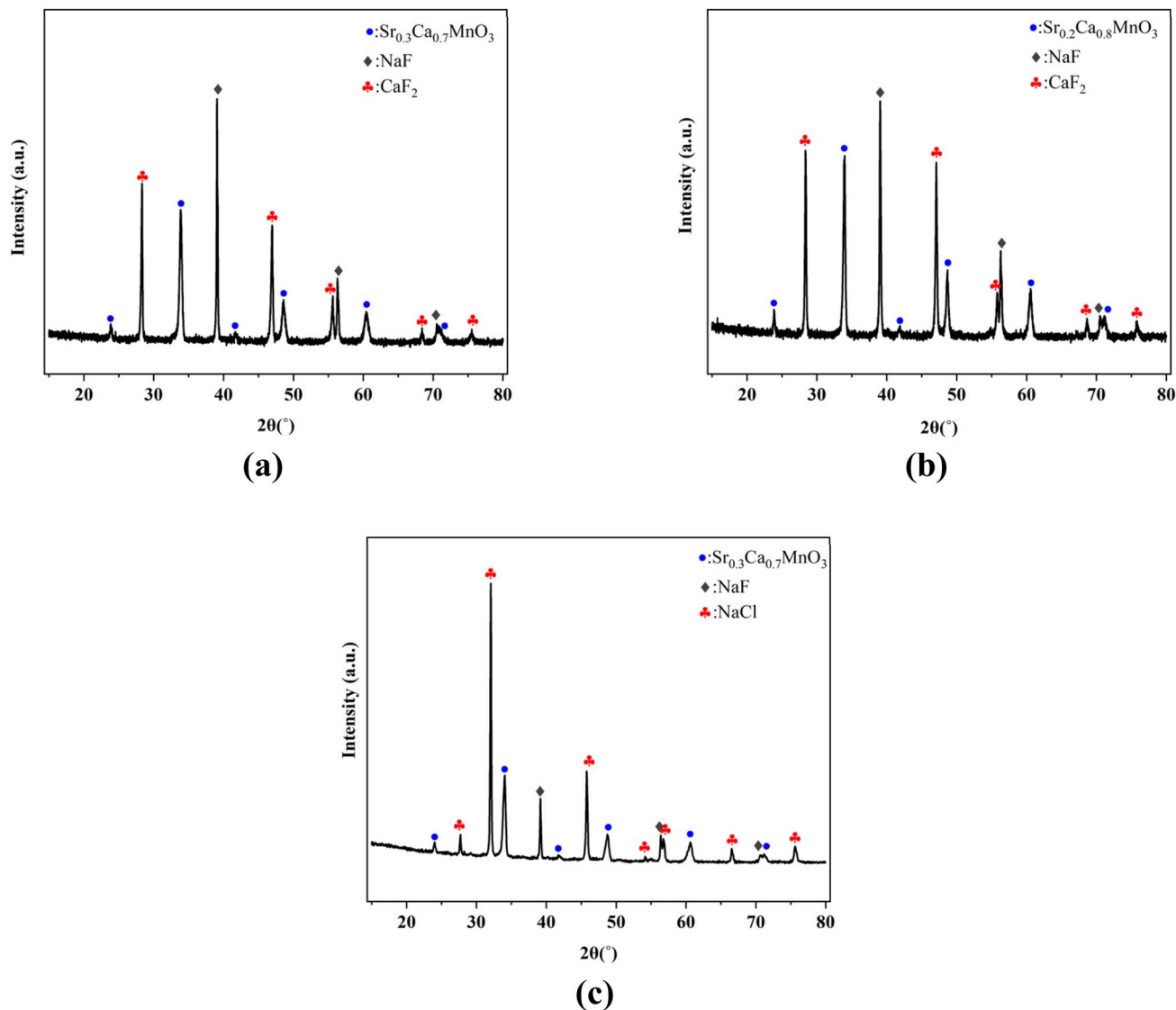*J. Mater. Chem. A*, 2025, **13**, 20028–20043 | **20031**

Fig. 2 XRD patterns of composite materials with Ca-based perovskites (a) SCFM1:NaF−CaF$_2$, (b) SCFM2:NaF−CaF$_2$ and (c) SCFM2:NaF−NaCl.

material with LiF–NaF–CaF$_2$ while the latter couldn't. A similar case that supports the high stability of La-based perovskite oxides was observed for Li$_2$CO$_3$–Na$_2$CO$_3$. The carbonate salt formed a compatible composite with a La-based material while a reaction with a Sr-based oxide occurred, causing incompatibility. Regarding the composites containing Li$_2$MoO$_4$, a minor peak of SrMoO$_4$ was detected from a possible reaction between LSF2 and Li$_2$MoO$_4$, whereas there seemed to be better compatibility for LSF1: Li$_2$MoO$_4$.

In our previous high-throughput study, we showed that among the substituted SrFeO$_{3-\delta}$-based materials, SCFM2 achieved the highest thermochemical energy density.[38] Due to the high redox activity of SCFM2, SCFM-based composites stored heat in both thermochemical and latent forms. On the other hand, LSF-based composites have shown better compatibility with various metal oxides and higher stability in the long term. Considering that many waste streams contain reducible gases such as H$_2$ and CO, we extended the application of LSF-based

composites for chemical energy recovery from the waste gas. Therefore, SCFM and LSF-containing composites were focused upon, with further details provided in Sections 3.2 and 3.3.

3.2 SCFM-based composite materials

3.2.1 Phase change properties and redox activity. Here, we assessed the latent heat and melting/solidification points of the composite materials under redox cycling conditions, the key parameters for thermal energy storage of molten salts.[21,25] The significant results for SCFM-based composites are summarized in Table 4, with additional data in Table S2 and Fig. S3–S9.† This evaluation was essential in confirming that phase change properties of composite materials align with those of the individual salts, thereby validating the compatibility between salt and perovskites. For example, SCFM2:NaF–NaCl exhibited a large discrepancy between the theoretical salt properties and measured properties of the composite, suggesting a potential
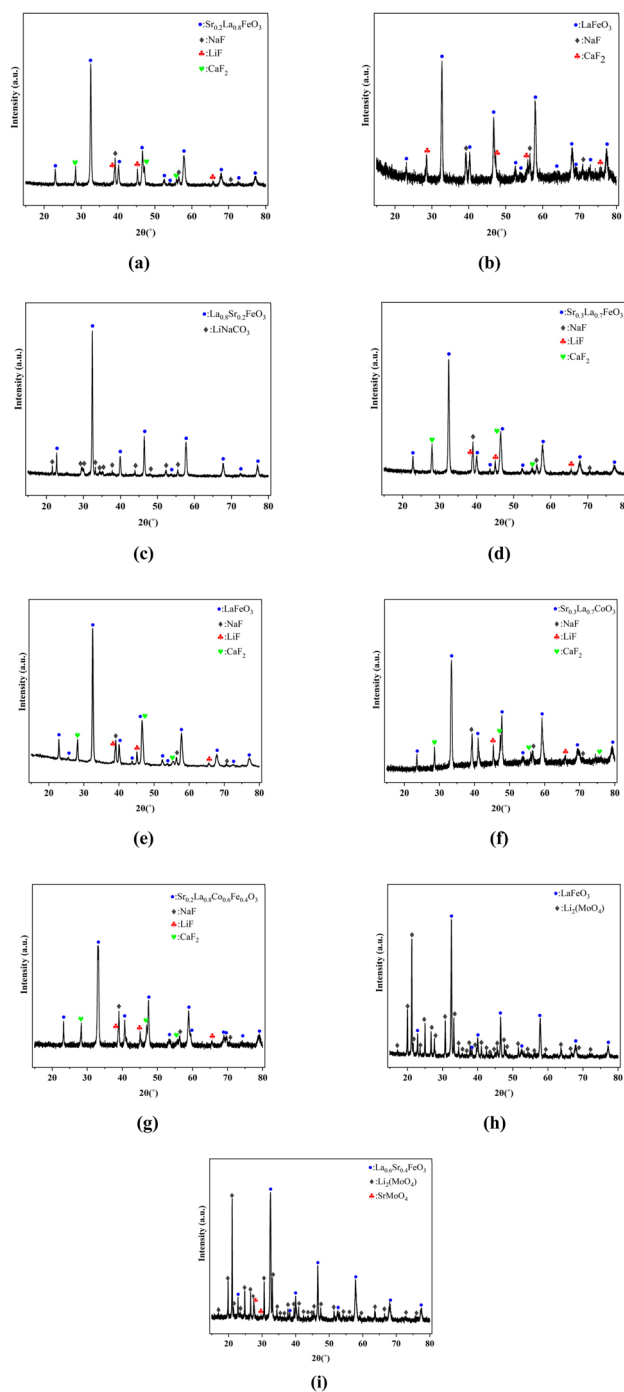
20032 | J. Mater. Chem. A, 2025, 13, 20028–20043

This journal is © The Royal Society of Chemistry 2025

Fig. 3 XRD patterns of composite materials with La-based perovskites (a) LSF1:LiF−NaF−CaF$_2$, (b) LSF1:MgF$_2$−NaF−CaF$_2$, (c) LSF1:Li$_2$CO$_3$−Na$_2$CO$_3$, (d) LSF2:LiF−NaF−CaF$_2$, (e) LSF3:LiF−NaF−CaF$_2$, (f) LSCM7391:LiF−NaF−CaF$_2$, (g) LSFCo:LiF−NaF−CaF$_2$, (h) LSF1:Li$_2$MoO$_4$ and (i) LSF2:Li$_2$MoO$_4$.

reaction between salt and perovskite during redox cycling; further details are provided in the ESI.† Meanwhile, the composite material SCFM2:NaF−CaF$_2$ with a weight ratio of 0.4 : 0.6 has shown promising performance in terms of high latent heat of ∼532 kJ kg$_{salt}^{-1}$ (mechanical stability information can be found in Section 5 of the ESI†). The measured latent heat

for the composite material was slightly lower than that of pure salt, as shown in Table 4. It should be noted that variations up to ±10% in repeated measurements were observed, likely due to differences in the Pt pan geometry and varied contact between the salt and the inert material at the bottom of the pan. Also, the melting point of the composite (798 °C) was measured to be slightly lower than that of pure salt (∼805 °C).

In addition, we examined the redox activity of the SCFM2:NaF−CaF$_2$, associated with O$_2$ release and uptake of the perovskite oxides during the reduction and oxidation steps, respectively. Upon switching from Ar to 20% O$_2$/Ar, an oxidation capacity of 1.05 wt% per oxide was determined. This was slightly less than the redox capacity (1.13 wt%) of pure perovskite under the same conditions (Fig. S7†), indicating that molten salt may slightly inhibit oxygen diffusion and exchange. When the atmosphere was returned to Ar, the reduction capacity matched the oxidation, indicating a reversible oxygen exchange behavior. Using the previously obtained enthalpy data of SCFM2, a thermochemical energy density of ∼105 kJ kg$_{oxide}^{-1}$ (∼42 kJ kg$_{composite}^{-1}$) was calculated. With the contributions from the sensible heat of salt and oxide, an overall energy density of ∼523 kJ kg^{-1} (4th cycle) was determined. Although the contribution of thermochemical energy was less than latent heat, using a redox-active support material instead of an inert material was advantageous for the overall energy density of the composite.

We evaluated the stability of phase change properties and redox activity in SCFM2:NaF−CaF$_2$ (0.4 : 0.6). Under a temperature swing of 740−890 °C, the composite exhibited a weight loss of 3.92 wt% (5.88 wt% per salt) over 10 redox cycles, which can be attributed to the evaporation of fluoride salt due to high vapor pressures.[52] However, the weight loss was still significantly lower than the loss of ∼10.2 wt% in the pure salt under similar conditions (Fig. S3†), indicating that perovskite stabilizes the fluoride salt by inhibiting its evaporation. To further decrease this loss, the experiments were conducted under a swing between 670−820 °C, with a layer of YSZ particles covering the composite. As shown in Fig. S4−S6† and 4a, both the composite material and salt demonstrated more stable performance under this lower temperature range. Over 10 cycles, the latent heat decreased from ∼532 to ∼513 kJ kg$_{salt}^{-1}$ in the composite. The redox capacity of SCFM2 also gradually declined from 1.05 to 0.56 wt% (per oxide) over the 10 cycles (Fig. 4b), possibly due to the partial decomposition of SCFM2 or the fluoride salt suppressing oxygen diffusion. Despite the slight deactivation, the overall energy density of the composite material remained high after 10 cycles (∼501 kJ kg^{-1}).

3.2.2 Long-term performance evaluation. Despite the slight deactivation of SCFM2:NaF−CaF$_2$ over 10 cycles, its good redox activity and large latent heat capacity made it an interesting candidate for long-term performance evaluation. As shown in Fig. 5a and S8,† the overall energy density decreased from ∼523 to ∼430 kJ kg^{-1} over 100 cycles under the conditions of 670 °C/ 20% O$_2$−820 °C/Ar, with a 23% reduction in latent heat. This deactivation is likely due to the evaporation of the fluoride salt, as indicated by an 11.6 wt% loss, suggesting that SCFM2 was unable to fully stabilize the NaF−CaF$_2$ salt material. Choosing a salt mixture with a lower melting point could potentially

This journal is © The Royal Society of Chemistry 2025

J. Mater. Chem. A, 2025, **13**, 20028−20043 | **20033**

Table 3 The summary of compatibility between salt mixtures and metal oxides *Undesirable phases are highlighted in italic*

Salt mixture	Perovskite	XRD phases	Compatibility (yes/no)
Li_2CO_3–Na_2CO_3	SBF	Na_2CO_3 $SrFeO_{2.6}$, *$SrCO_3$, $Li_{1.05}Fe_{0.95}O_2$, $Sr_2Fe_3O_6$, Na_3FeO_3*	N
	LSF1	$La_{0.8}Sr_{0.2}FeO_3$, $LiNaCO_3$	Y
LiF–NaF–CaF_2	CAM	CaF_2, NaF, Ca_2AlMnO_5, *Li_2MnO_3, CaO, $LiAlO_2$, $CaMn_7O_{12}$*	N
	SF	NaF, $Sr_{0.88}Ca_{0.08}Na_{0.02}Fe_{0.02}F_2$, *$Li_{1.05}Fe_{0.95}O_2$, CaO, FeF_3*	N
	SBF	NaF, $Sr_{0.88}Ca_{0.08}Na_{0.02}Fe_{0.02}F_2$, *$Li_{0.5}Fe_{0.5}O_2$, $Ca_{0.5}Sr_{0.5}FeO_2$, $LiFeO_2$, $LiBaF_3$, $Sr_3Fe_2O_6$*	N
	SCMCo1	NaF, CaF_2, $CaMnO_3$, *Li_2MnO_3*	N
	SCMCo2	NaF, CaF_2, $CaMnO_{2.656}$, *$Li_{1.33}Mn_{0.667}O_2$*	N
	LSF1	$La_{0.8}Sr_{0.2}FeO_3$, CaF_2, NaF, LiF	Y
	LSF2	$La_{0.7}Sr_{0.3}FeO_3$, CaF_2, NaF, LiF	Y
	LSF3	$LaFeO_3$, CaF_2, NaF, LiF	Y
	LSCoM2	$La_{0.7}Sr_{0.3}CoO_3$, CaF_2, NaF, LiF	Y
	LSCoM1	NaF, $Sr_{0.4}La_{0.6}CoO_3$, *$Sr_{0.5}Ca_{0.5}F_2$, $LiCoO_2$*	N
	LSFCo	$La_{0.8}Sr_{0.2}Co_{0.6}Fe_{0.4}O_3$, CaF_2, NaF, LiF	Y
NaF–CaF_2	SCFM1	$Sr_{0.3}Ca_{0.7}MnO_3$, NaF, CaF_2	Y
	SCFM2	$Sr_{0.2}Ca_{0.8}MnO_3$, NaF, CaF_2	Y
MgF_2–NaF–CaF_2	SCFM1	CaF_2, $Sr_{0.5}Ca_{0.5}MnO_3$, NaF, *$Na_{0.15}Ca_{0.85}F_{1.85}$, $CaFe_2O_4$, $Na_{0.457}Fe_{0.67}Mn_{0.33}O_2$*	N
	LSF1	$La_{0.6}Sr_{0.4}FeO_{2.997}$, CaF_2, NaF	Y
NaF–NaCl	SCFM2	$Sr_{0.3}Ca_{0.7}MnO_3$, NaF, NaCl	Y
NaF-KF	SCFM2	NaF, $CaMnO_3$, *$KCaF_3$, $K_3NaFe_2O_8$*[b]	N
	CAM	NaF, *$CaMnO_{2.97}$, Ca_2MnO_4, $CaAl_2O_4$, $KCaF_3$, $KAlO_2$*	N
LiF–CaF_2	SCFM1	CaF_2, *$Li_{1.259}Mn_{0.519}Fe_{0.225}O_2$*	N
LiF–NaF	SF	$SrFeO_{2.6}$, LiF, NaF, *SrF_2, $LiFeO_2$, $Sr_3Fe_2O_7$, FeF_3, Fe_3O_4*[b]	N
	SBF	LiF, NaF, *SrF_2, $Li_{0.5}Fe_{0.5}O$, Fe_2O_3*[b]	N
Li_2MoO_4	LSF1	Li_2MoO_4, $LaFeO_3$	Y
	LSF2	Li_2MoO_4, $La_{0.6}Sr_{0.4}FeO_3$, *$SrMoO_4$*	Y[a]

[a] Trace amount of $SrMoO_4$ was detected. [b] Minor unidentified peaks were present in the XRD pattern.

Table 4 Measured melting enthalpy (kJ kg_{salt}^{-1}) and melting points (°C) of composite materials. *The weight ratios of eutectic salt mixtures are provided in* Table 2

Sample name (weight ratio)	Melting enthalpy (kJ kg_{salt}^{-1})		Melting temperature (°C)	
	Reported	Measured (±10%)	Reported	Measured
NaF–CaF_2	560–600	561.80	810	804.67
NaF–CaF_2:SCFM2 (0.4 : 0.6)	560–600	532.47	810	797.91
NaF–NaCl:SCFM2 (0.5 : 0.5)	572	340.84	674	672.13

enhance the stability of ROMS composites by lowering the thermal losses.

On the other hand, SCFM2 maintained its redox activity, although the redox capacity gradually decreased from ~1.05 wt% to ~0.45 wt%, reducing thermochemical heat from ~105 to ~50 kJ kg_{oxide}^{-1} (~42 to ~20 kJ $kg_{composite}^{-1}$) over 100 cycles. Post-experimental XRD (Fig. S33†) showed that the reduced perovskite was transitioned to a Brownmillerite phase ($Sr_2Fe_2O_5$) with additional minor peaks suggesting the partial decomposition of the oxide, which would explain the decrease in thermochemical heat. However, phase identification was challenging due to the presence of inert material that could not be fully separated from the sample. Nevertheless, the XRD results indicated that compatibility between salt and oxide was maintained after 100 redox cycles. Despite the deactivation of SCFM2:NaF–CaF_2, these results support the hypothesis that molten salts and perovskite oxides can be compatible, storing

heat *via* both phase change of the molten salt and redox reactions of the metal oxide.

3.3 LSF-based composite materials

3.3.1 Phase change properties and redox-activity. Most of the compatible composite materials included La-containing perovskites due to their stability in the presence of salt mixtures. In SCFM2:NaF–CaF_2, the high melting point of the salt restricted the operating temperature to higher temperatures (>670 °C). Meanwhile, La-based perovskites paired with lower melting point salts enabled lower operating temperatures, reducing thermal losses. The summary of the measurements for LSF-based composites is presented in Table 5 below, with additional data in Fig. S10–S25 and Table S2.†

Our results revealed that the oxide : salt ratio has a significant impact on the phase change property of the composite materials. Fig. 6 demonstrates that melting enthalpy for
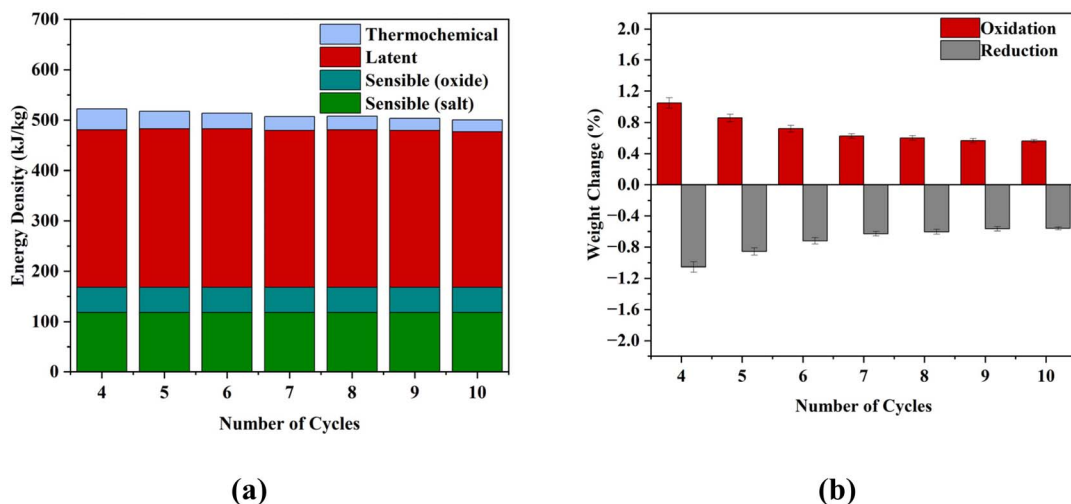
20034 | *J. Mater. Chem. A*, 2025, **13**, 20028–20043

This journal is © The Royal Society of Chemistry 2025

Fig. 4 TGA-DSC measurements for SCFM2:NaF−CaF$_2$ with the weight ratio of 0.4 : 0.6 at 670 °C/20% O$_2$−820 °C/Ar during 10 cycles. (a) Overall energy density (kJ kg^{-1}), (b) weight change (%) normalized to the weight of SCFM2. *Latent heat is the measured melting enthalpy from DSC. Thermochemical heat is calculated using the previous data on SCFM2.*[38] *Sensible heat is based on estimated heat capacities through an additive principle using NIST database.*[62]
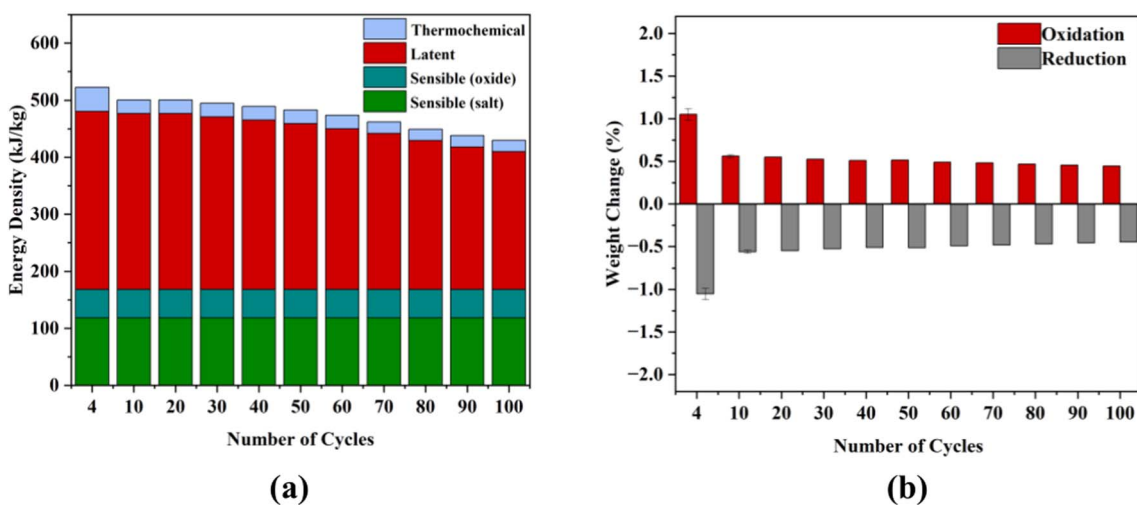

Fig. 5 TGA-DSC measurements for SCFM2:NaF−CaF$_2$ with the weight ratio of 0.4 : 0.6 at 670 °C/20% O$_2$−820 °C/Ar during 100 cycles. (a) Overall energy density (kJ kg$_{composite}$$^{-1}$), (b) weight change (%) normalized to the weight of SCFM2). *Latent heat is the measured melting enthalpy from DSC. Thermochemical heat is calculated using the previous data on SCFM2.*[38] *Sensible heat is based on estimated heat capacities through additive principle using NIST database.*[62]

LSF1:LiF−NaF−CaF$_2$ decreases with increasing oxide content. While the melting enthalpy of pure LiF−NaF−CaF$_2$ was measured as ∼623 kJ kg$_{salt}$$^{-1}$, it dropped to ∼580 kJ kg$_{salt}$$^{-1}$ when mixed with LSF1 at an oxide : salt ratio of 0.4 : 0.6. Similar trends were also observed for the composites of NaF−CaF$_2$:-SCFM2, LSFC:LiF−NaF−CaF$_2$, and LSF2:Li$_2$MoO$_4$. Since the absence of chemical interaction between the salt and oxide phase was confirmed by XRD, the decrease in the latent heat with increasing salt content can be attributed to physical interactions. Previous research has also observed latent heat reduction in a porous supporting medium and linked this to the confinement of the phase change material.[63–65] Additionally, melting temperatures also decreased with increasing oxide

contents, consistent with the previous findings.[27,64,66] The LSF-based composite materials with the other salts either faced stability issues or did not have a competitive energy density due to low latent heat, as briefly discussed in the ESI† (for LSF1:Li$_2$CO$_3$−Na$_2$CO$_3$ and LSF1:LiF−NaF−MgF$_2$).

In terms of redox activity, most of the La-based perovskites in the composite materials failed to exchange their lattice oxygen during the redox cycles due to: (i) the intrinsic stability of these perovskite oxides, and (ii) the additional mass transfer resistance due to the presence of the salt. While pure LSFCo showed a redox capacity of ∼0.08 wt%, no significant weight change was observed for LSFCo in the composite (Fig. S18†). Noting that the temperature range was not high enough to activate the redox

This journal is © The Royal Society of Chemistry 2025

J. Mater. Chem. A, 2025, **13**, 20028–20043 | **20035**

Table 5 Measured melting enthalpy (kJ kg$_{salt}^{-1}$) and melting points (°C) of composite materials. *The weight ratios of eutectic salt mixtures are provided in* Table 2

Sample name (weight ratio)	Melting enthalpy (kJ kg$_{salt}^{-1}$)		Melting temperature (°C)	
	Reported	Measured (error bar ±10%)	Reported	Reported
LiF–NaF–CaF$_2$	640	622.93	615	609.69
LSF1:LiF–NaF–CaF$_2$ (0.5 : 0.5)	640	542.73	615	603.36
LSF1:LiF–NaF–CaF$_2$ (0.4 : 0.6)	640	579.74	615	606.66
LSF2:LiF–NaF–CaF$_2$ (0.5 : 0.5)	640	544.00	615	600.06
LSF3:LiF–NaF–CaF$_2$ (0.5 : 0.5)	640	466.54	615	600.88
LSCoM2:LiF–NaF–CaF$_2$ (0.5 : 0.5)	640	549.55	615	605.17
LSFCo:LiF–NaF–CaF$_2$ (0.5 : 0.5)	640	537.41	615	602.98
LSFCo:LiF–NaF–CaF$_2$ (0.4 : 0.6)	640	595.05	615	606.73
Li$_2$MoO$_4$	280	281.49	705	693.40
LSF1:Li$_2$MoO$_4$ (0.5 : 0.5)	280	254.59	705	685.08
LSF2:Li$_2$MoO$_4$ (0.5 : 0.5)	280	252.46	705	687.55
LSF2:Li$_2$MoO$_4$ (0.6 : 0.4)	280	219.95	705	688.18

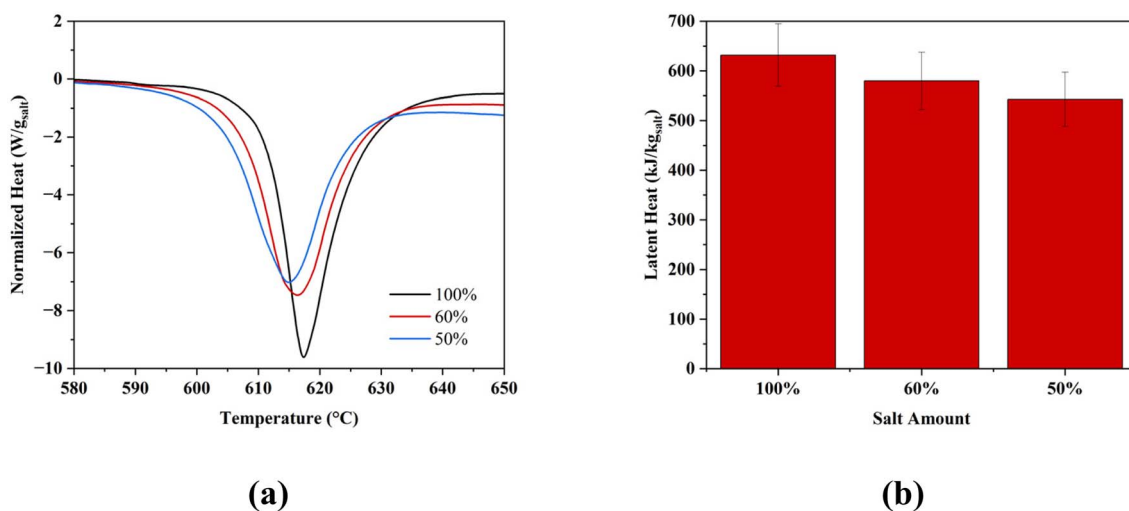**Fig. 6** Comparison of LSF1:LiF–NaF–CaF$_2$ at various salt amounts. (a) Normalized heat flows (W g$_{salt}^{-1}$) and (b) latent heats (kJ kg$_{salt}^{-1}$)

behavior of La-based perovskite. Previous studies have shown that La-based perovskite can achieve high reaction enthalpy and oxygen capacity at elevated temperatures.[67,68] Among the LSF-based composites, only LSF2 exhibited a weight gain corresponding to oxidation (Fig. S13, S22 and S23†). Increased Sr : La ratio was found to benefit the redox activity by lowering the reduction temperature but also increased the likelihood of chemical interactions with the salt. In LSF2:Li$_2$MoO$_4$, the redox capacity increased from ∼0.08 to ∼0.15 wt% per oxide with oxide content increasing from 50 to 60%. Optimizing the oxide microstructure can potentially decrease the mass transfer resistance but LSF-based composites require a more reducing environment (*e.g.* higher temperatures or reducing gases) in order to exhibit substantial redox capacity. This will be further discussed in a later section.

3.3.2 Long-term performance evaluation. Due to its high latent heat storage and compatibility, LSF1:LiF–NaF–CaF$_2$ with the weight ratio of 0.4 : 0.6 was selected as a promising

candidate for long-term performance evaluation (see Section 5 in ESI† with respect to mechanical stability). As shown in Fig. 7, the composite demonstrated excellent stability over 100 cycles under the conditions of 510 °C/20% O$_2$–660 °C/Ar, with no significant change in the latent heat. The good stability of this composite material can be attributed to its lower operating temperature range compared to that of SCFM2:NaF–CaF$_2$. The addition of LiF to NaF–CaF$_2$ lowers the melting point, thus allowing for a lower operating temperature range and preventing salt weight loss from evaporation. Since no O$_2$ release/ uptake was observed, there was no thermochemical energy contributed to the overall energy density. After 100 cycles, the total energy density, including latent and sensible heat, remained as high as ∼534 kJ kg^{-1}.

Additionally, we compared the XRD pattern of the LSF1:LiF– NaF–CaF$_2$ before and after 100 cycles in Fig. 8a. The additional peak corresponds to the thin layer of YSZ, which covered the bottom of the pan during the experiment. No significant change
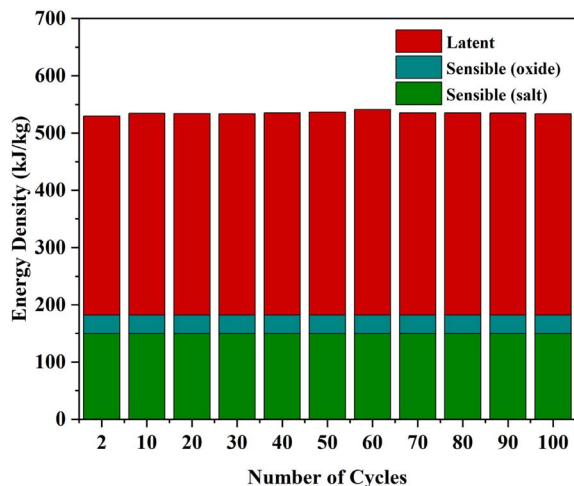
20036 | *J. Mater. Chem. A*, 2025, **13**, 20028–20043

This journal is © The Royal Society of Chemistry 2025

Fig. 7 TGA-DSC measurements for LSF1:LiF−NaF−CaF$_2$ with the weight ratio of 0.4 : 0.6 at 510 °C/20% O$_2$−660 °C/Ar during 100 cycles. (a) Overall energy density (kJ kg^{-1}). *Latent heat is the measured melting enthalpy from DSC. Sensible heat is based on estimated heat capacities through additive principle using NIST database.*[62]

in the phases of perovskite and salts was seen. This shows that no reactions between LSF and fluoride salt occurred during redox cycles, thus the ROMS composite maintained its compatibility and energy density during 100 cycles. According to Fig. 8b and c, the morphology of the composite material was also maintained after 100 cycles (EDX mappings can be found in Fig. S36†).

3.3.3 Thermal conductivity. For LSF1: LiF−NaF−CaF$_2$ (0.4 : 0.6), we also measured thermal conductivity, a key factor in heat transfer efficiency.[11,14] Table 6 presents the measured thermal conductivities and compares them with other composite materials reported for thermal energy storage. Using the transient plane source principle, the thermal conductivity of LSF1: LiF−NaF−CaF$_2$ (0.4 : 0.6) was found to be 2.51 W m^{-1} K^{-1}, which falls within the range of measured thermal conductivities of individual components. While LSF1 showed relatively low thermal conductivity, consistent with the results of other metal oxides in the literature,[69,70] the elevated thermal conductivity of fluoride salt led to a competitively high thermal conductivity for the composite material compared to some other reported composites. The high thermal conductivity of the ROMS

(a)
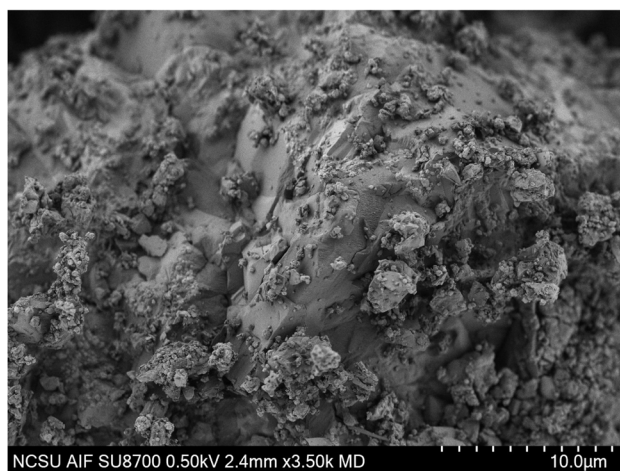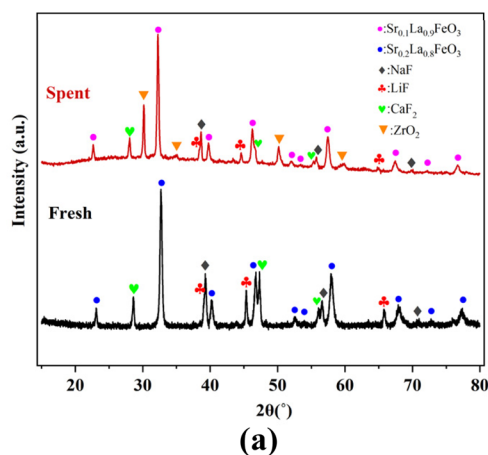
(b)
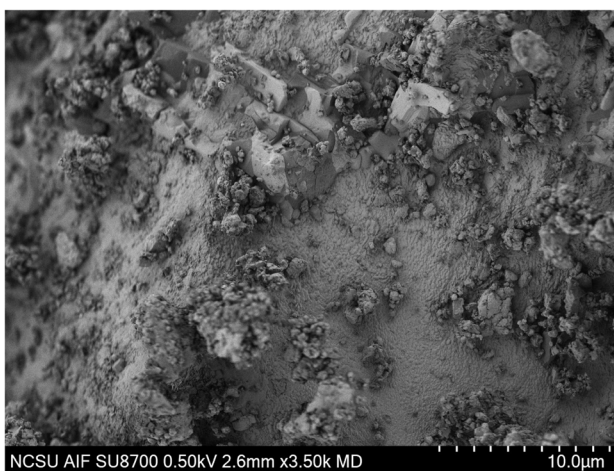
(c)

Fig. 8 Comparison of fresh and spent (after 100 cycles between 510 °C/20% O$_2$−660 °C/Ar) LSF1:LiF−NaF−CaF$_2$ (0.4 : 0.6). (a) XRD patterns and SEM images of (b) after sintering, *which corresponds to the morphology of composite material after 1 cycle* (c) after 100 cycles.

This journal is © The Royal Society of Chemistry 2025

J. Mater. Chem. A, 2025, **13**, 20028–20043 | **20037**

Table 6 Comparison of thermal conductivities at room temperature

| Material	Thermal conductivity (W m^{-1} K^{-1})	Measurement method
LSF1	0.76	Transient
LiF–NaF–CaF$_2$	2.96	Transient
LSF1:LiF–NaF–CaF$_2$ (0.4 : 0.6)	2.51	Transient
LiNO$_3$–NaNO$_3$–KNO$_3$–Ca(NO$_3$)$_2$:calcium silicate[11]	1.18	Steady state
NaNO$_3$: modified diatomite[25]	∼0.28	Transient
Li$_2$CO$_3$–Na$_2$CO$_3$:MgO:carbon[23]	∼3–5.25	Transient
Polyethylene glycol:diatomite: expanded graphite[28]	0.32–0.67	Transient

composite enables rapid heat exchange, enhancing adaptability in various reactor designs.

3.3.4 Alternative applications under a reducing gas environment. Despite the stable performance of LSF1:LiF–NaF–CaF$_2$ composite, the limited redox performance of La-based perovskites decreases the overall energy density. To address this, we explored an alternative usage of ROMS composites. The exhaust gas emitted by electric arc furnaces or blast furnaces in the steel industry carries substantial waste heat, often rich in reducing agents like H$_2$ and CO[8,71,72] which holds valuable potential for thermochemical energy storage applications. Thus, we performed experiments under a reducing gas atmosphere for a composition with Li$_2$MoO$_4$ since previous research indicated Mo salts in the liquid phase improve oxygen diffusion.[73] Although LSF2 exhibited better potential for redox activity than LSF1 under cyclic conditions between 20% O$_2$–Ar, LSF2:Li$_2$MoO$_4$ was not tested due to the trace amount of SrMoO$_4$ impurity detected in its XRD pattern (Fig. 3i). Therefore, LSF1:Li$_2$MoO$_4$ (0.5 : 0.5) was tested as a potential candidate, with the results presented in Fig. 9 and S26–S32.†

LSF1:Li$_2$MoO$_4$ (0.5 : 0.5) achieved thermochemical energy storage capacity as high as 1813 kJ kg^{-1} after a sufficiently long reduction time (∼8 h) to reach equilibrium. However, in electric arc furnaces, tap-to-time per batch is typically much shorter, around 30–70 min[8,72] When a shorter reduction time of 35 min applied, the composite material still achieved an excellent thermochemical energy storage capacity of ∼664 kJ kg^{-1}. Comparing this to the oxidation enthalpies of LSF1(∼239 kJ kg^{-1}) and Li$_2$MoO$_4$ (∼683 kJ kg^{-1}) (Table 7), it appears that the redox activity of Li$_2$MoO$_4$ primarily enhanced the energy storage capacity of LSF1: Li$_2$MoO$_4$ rather than LSF1. Additionally, reduction kinetics, shown in Fig. 9, indicate that rapid weight loss in LSF1: Li$_2$MoO$_4$ was mainly attributable to the fast reduction kinetics of Li$_2$MoO$_4$. The fast kinetics resulted in a ROMS composition with improved thermochemical energy compared to pure LSF1. Including the estimated sensible heat and latent heat, the overall energy density for LSF1: Li$_2$MoO$_4$ (0.5 : 0.5) reached 875 kJ kg^{-1}.

While Li$_2$MoO$_4$ exhibited rapid weight loss, weight gain didn't match weight loss in Li$_2$MoO$_4$, potentially caused by slow oxidation kinetics as shown in Fig. S28.† Meanwhile weight loss and gain were approximately the same in LSF1 and LSF1: Li$_2$MoO$_4$, indicating reversible redox behaviors. This indicates that mixing LSF1 and Li$_2$MoO$_4$ created a synergistic benefit:
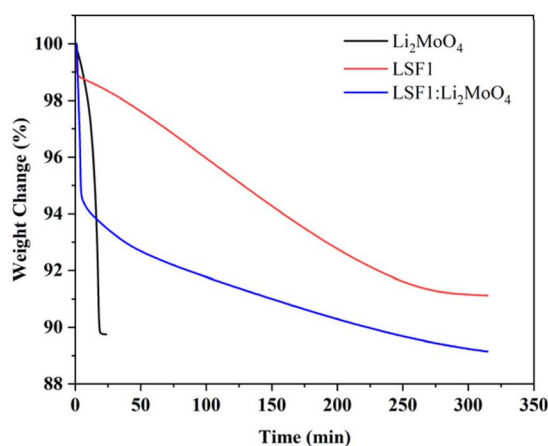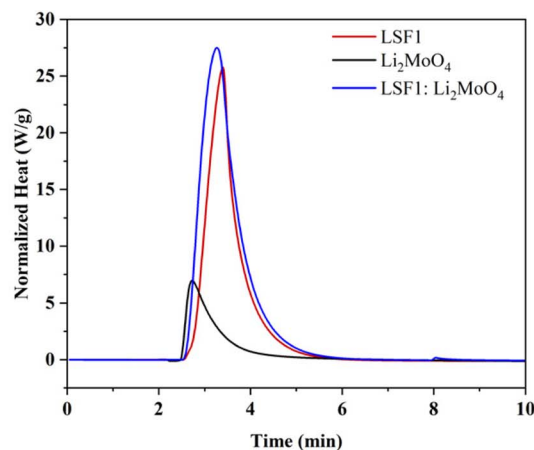
Fig. 9 Comparison of LSF1, Li$_2$MoO$_4$, and LSF1:Li$_2$MoO$_4$ with the weight ratio of 0.5 : 0.5 during long reduction. (a) Weight changes (%) at 730 °C/20% H$_2$ and (b) heat flow (mW) at 580/20% O$_2$.

20038 | *J. Mater. Chem. A*, 2025, **13**, 20028–20043

This journal is © The Royal Society of Chemistry 2025

Table 7 Weight changes (%) and energy densities of LSF1, Li_2MoO_4, and LSF1:Li_2MoO_4 (0.5 : 0.5). *Weight loss and weight gain correspond to the weight changes in the samples during gas switch to 20% H_2 and 20% O_2, respectively*

Material	Weight loss (wt%)	Weight gain (wt%)	Oxidation enthalpy (kJ kg^{-1}) ±10%	Overall energy density (kJ kg^{-1})
Li_2MoO_4	10.0	8.17	682.7	1051
LSF1 (short reduction)	2.10	2.49	238.9	319.4
LSF1 (long reduction)	8.90	8.85	1309	1389
LSF1:Li_2MoO_4 (short reduction)	6.37	6.39	664.1	874.7
LSF1:Li_2MoO_4 (long reduction)	11.5	11.5	1813	2024

LSF1 facilitates rapid oxidation and Li_2MoO_4 drives fast reduction. As can be seen from Fig. S31 and S32,† in a cyclic experiment, the fast reduction and oxidation behavior of LSF1:Li_2MoO_4 with the weight ratio of 0.6 : 0.4 was maintained. While a detailed understanding of the reduction and oxidation mechanisms for this interesting composite is beyond the scope of this study, its promising performance can encourage future research aimed at recovering waste heat.

4. Comparison of ROMS composites

As can be seen from Table 8, ROMS composites offer superior thermal energy storage performance compared to phase change composites with inert skeletons. They can achieve higher energy densities within narrower temperature ranges. Fig. 10 compares the thermal energy densities of three ROMS composite materials with different performance features. LSF1:LiF–NaF–CaF$_2$ exhibited the highest latent heat capacity of 580 kJ kg$_{salt}^{-1}$ though it showed no redox activity under a pressure swing between 20% O$_2$–Ar, leading to a total energy density of ~530 kJ kg$_{composite}^{-1}$ over a relatively low-temperature range (510–660 °C). Meanwhile, SCFM2:NaF–CaF$_2$ exhibited both thermochemical and latent heat based energy storage. Still, latent heat storage was the main contributor to its overall energy density of ~523 kJ kg^{-1} under the cycling conditions of 670/20% O$_2$–820 °C/Ar. Lastly, LSF1:Li_2MoO_4 achieved the highest overall energy density up to 875 kJ kg^{-1} at 580/20% O$_2$–730 °C/20% H$_2$, driven primarily by redox activity of both salt and oxide. This material is proposed for harnessing fuel containing off-gas from the steel industry. In terms of sensible heat storage, LiF–NaF–CaF$_2$ had the highest capacity among salts, reaching 250 kJ kg$_{salt}^{-1}$, while SCFM2 was expected to achieve the highest among oxides, at
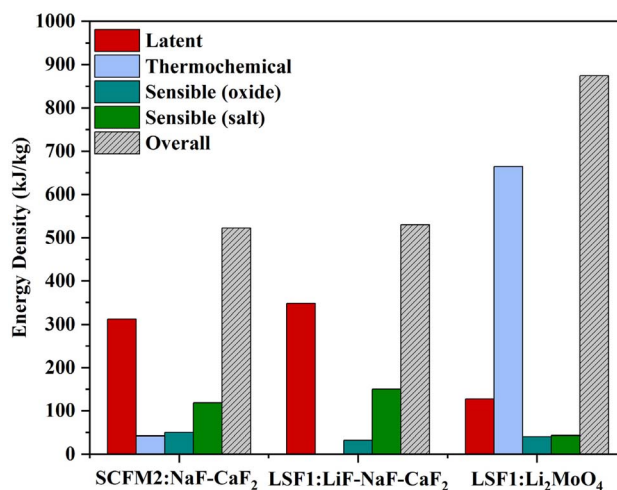

Fig. 10 Comparison of energy densities for SCFM2:NaF–CaF$_2$ (0.4 : 0.6), LSF1:LiF–NaF–CaF$_2$ (0.4 : 0.6), and LSF1: Li_2MoO_4 (0.5 : 0.5) under the redox cycling conditions of 670/20% O$_2$–820 °C/Ar, 510/20% O$_2$–660 °C/Ar, and 580/20% O$_2$–730 °C/20% H$_2$, respectively. *The units of kJ kg$_{composite}^{-1}$ were used for each component. Sensible heat is based on estimated heat capacities through additive principle using NIST database.*[62]

~125 kJ kg$_{oxide}^{-1}$. LSF1:LiF–NaF–CaF$_2$ showed excellent stability and robustness over 100 cycles, whereas SCFM2:NaF–CaF$_2$ showed deactivation with a gradual decline in latent and thermochemical heat over time. LSF1: Li_2MoO_4 showed good stability over the 5 cycles tested under a more reducing atmosphere.

5. Conclusions

This study introduces redox-active oxide-molten salt (ROMS) composites, where a porous perovskite oxide serves as a support to prevent salt leakage. This novel family of materials has the potential to utilize both latent heat from the phase transition of salt and thermochemical heat from the redox reactions to achieve high energy density within narrow temperature swings. Among 25 tested perovskite–salt combinations, 12 were found to be compatible with La-based perovskites showing superior compatibility and Sr and/or Ca-containing oxides exhibiting good redox activity. SCFM6271:NaF–CaF$_2$ (0.4 : 0.6) was identified for both phase transition and redox-based energy storage with an overall capacity of ~523 kJ kg^{-1} (670–820 °C) but faced

Table 8 Comparison of energy densities storage densities over the corresponding temperature ranges

Material	Energy storage density (kJ kg^{-1})	Temperature range (°C)
SCFM2:NaF–CaF$_2$	523	670–820
LSF1:LiF–NaF–CaF$_2$	530	510–660
LSF1:Li_2MoO_4	875	580–730
NaNO$_3$: Modified diatomite[25]	383	130–330
NaNO$_3$:Ca(OH)$_2$[74]	265–468	140–340
Graphite:Na$_2$CO$_3$–Li$_2$CO$_3$: MgO[27]	525	300–600
NaCl–KCl:diatomite[10]	393	550–750

This journal is © The Royal Society of Chemistry 2025

J. Mater. Chem. A, 2025, **13**, 20028–20043 | **20039**

stability and deactivation issues over the long term. Meanwhile, LSF1:NaF–CaF$_2$–LiF (0.4 : 0.6) maintained a latent heat-based energy storage capacity of ~530 kJ kg^{-1} although it did not exhibit redox activity under the cycling conditions of 510/20% O$_2$–660 °C/Ar. It demonstrated excellent stability over 100 cycles, while compatibility and morphology were also maintained. The thermal conductivity of LSF1: LiF–NaF–CaF$_2$ was found to be 2.51 W m^{-1} K^{-1}. Lastly, LSF1: Li$_2$MoO$_4$ (0.5 : 0.5) exhibited high redox activity with an overall energy density up to ~875 kJ kg^{-1} and was proposed as a promising candidate for recovering waste gas streams rich in residue fuels. The interesting characteristics and versatility of the ROMS composites reported in this study can potentially find applications for various thermal energy storage scenarios.

Data availability

Data supporting this article have been included as part of the ESI.†

Conflicts of interest

There are no conflicts to declare.

Acknowledgements

References

1 Fossil Fuels, https://www.eesi.org/topics/fossil-fuels/description#:~:text=Fossil%20fuels%E2%80%94including%20coal%2C%20oil,percent%20of%20the%20world's%20energy, accessed 2024-03-08.

2 Fossil fuels account for the largest share of U.S. energy production and consumption, https://www.eia.gov/todayinenergy/detail.php?id=45096, accessed 2024-03-08.

3 Greenhouse gas emissions, https://ourworldindata.org/greenhouse-gas-emissions, accessed 2024-03-08.

4 C. Forman, I. K. Muritala, R. Pardemann and B. Meyer, Estimating the Global Waste Heat Potential, Renewable Sustainable Energy Rev., 2016, 57, 1568–1579, DOI: 10.1016/j.rser.2015.12.192.

5 M. Ja'fari, M. I. Khan, S. G. Al-Ghamdi, A. J. Jaworski and F. Asfand, Waste Heat Recovery in Iron and Steel Industry Using Organic Rankine Cycles, Chem. Eng. J., 2023, 477, 146925, DOI: 10.1016/j.cej.2023.146925.

6 L. Miró, J. Gasia and L. F. Cabeza, Thermal Energy Storage (TES) for Industrial Waste Heat (IWH) Recovery: A Review, Appl. Energy, 2016, 179, 284–301, DOI: 10.1016/j.apenergy.2016.06.147.

7 A. Vannoni, A. Sorce, A. Traverso and A. Fausto Massardo, Techno-Economic Optimization of High-Temperature Heat Pumps for Waste Heat Recovery, Energy Convers. Manage., 2023, 290, 117194, DOI: 10.1016/j.enconman.2023.117194.

8 I. Alshehhi, W. Alnahdi, M. Ali, A. Bouabid and A. Sleptchenko, Assessment of Waste Heat Recovery in the Steel Industry, J. Sustain. Dev. Energy Water Environ. Syst., 2023, 11(2), 1–22, DOI: 10.13044/j.sdewes.d10.0440.

9 F. Dal Magro, M. Jimenez-Arreola and A. Romagnoli, Improving Energy Recovery Efficiency by Retrofitting a PCM-Based Technology to an ORC System Operating under Thermal Power Fluctuations, Appl. Energy, 2017, 208, 972–985, DOI: 10.1016/j.apenergy.2017.09.054.

10 G. Leng, G. Qiao, Z. Jiang, G. Xu, Y. Qin, C. Chang and Y. Ding, Micro Encapsulated & Form-Stable Phase Change Materials for High Temperature Thermal Energy Storage, Appl. Energy, 2018, 217, 212–220, DOI: 10.1016/j.apenergy.2018.02.064.

11 Z. Jiang, G. Leng, F. Ye, Z. Ge, C. Liu, L. Wang, Y. Huang and Y. Ding, Form-Stable LiNO$_3$ –NaNO$_3$–KNO$_3$–Ca(NO$_3$)$_2$/Calcium Silicate Composite Phase Change Material (PCM) for Mid-Low Temperature Thermal Energy Storage, Energy Convers. Manage., 2015, 106, 165–172, DOI: 10.1016/j.enconman.2015.09.035.

12 I. Sarbu and C. Sebarchievici, A Comprehensive Review of Thermal Energy Storage, Sustainability, 2018, 10(1), 191, DOI: 10.3390/su10010191.

13 A. Caraballo, S. Galán-Casado, Á. Caballero and S. Serena, Molten Salts for Sensible Thermal Energy Storage: A Review and an Energy Performance Analysis, Energies, 2021, 14(4), 1197, DOI: 10.3390/en14041197.

14 T. Wang, D. Mantha and R. G. Reddy, Novel High Thermal Stability LiF–Na$_2$CO$_3$–K$_2$CO$_3$ Eutectic Ternary System for Thermal Energy Storage Applications, Sol. Energy Mater. Sol. Cells, 2015, 140, 366–375, DOI: 10.1016/j.solmat.2015.04.033.

15 R. Roper, M. Harkema, P. Sabharwall, C. Riddle, B. Chisholm, B. Day and P. Marotta, Molten Salt for Advanced Energy Applications: A Review, Ann. Nucl. Energy, 2022, 169, 108924, DOI: 10.1016/j.anucene.2021.108924.

16 T. Wang, D. Mantha and R. G. Reddy, Thermal Stability of the Eutectic Composition in LiNO$_3$–NaNO$_3$–KNO$_3$ Ternary System Used for Thermal Energy Storage, Sol. Energy Mater. Sol. Cells, 2012, 100, 162–168, DOI: 10.1016/j.solmat.2012.01.009.

17 R. W. Bradshaw and N. P. Siegel, Molten Nitrate Salt Development for Thermal Energy Storage in Parabolic Trough Solar Power Systems, in ES2008, ASME 2008 2nd International Conference on Energy Sustainability, 2008, vol. 2, pp. 631–637, DOI: 10.1115/ES2008-54174.

18 T. Wang, D. Mantha and R. G. Reddy, Novel Low Melting Point Quaternary Eutectic System for Solar Thermal Energy

20040 | J. Mater. Chem. A, 2025, 13, 20028–20043

This journal is © The Royal Society of Chemistry 2025

Storage, *Appl. Energy*, 2013, **102**, 1422–1429, DOI: **10.1016/j.apenergy.2012.09.001**.

19 J. Sunku Prasad, P. Muthukumar, F. Desai, D. N. Basu and M. M. Rahman, A Critical Review of High-Temperature Reversible Thermochemical Energy Storage Systems, *Appl. Energy*, 2019, **254**, 113733, DOI: **10.1016/j.apenergy.2019.113733**.

20 A. Awad, A. Burns, M. Waleed, M. Al-Yasiri and D. Wen, Latent and Sensible Energy Storage Enhancement of Nano-Nitrate Molten Salt, *Sol. Energy*, 2018, **172**, 191–197, DOI: **10.1016/j.solener.2018.04.012**.

21 M. M. Kenisarin, High-Temperature Phase Change Materials for Thermal Energy Storage, *Renewable Sustainable Energy Rev.*, 2010, **14**(3), 955–970, DOI: **10.1016/j.rser.2009.11.011**.

22 E. González-Roubaud, D. Pérez-Osorio and C. Prieto, Review of Commercial Thermal Energy Storage in Concentrated Solar Power Plants: Steam *vs.* Molten Salts, *Renewable Sustainable Energy Rev.*, 2017, **80**, 133–148, DOI: **10.1016/j.rser.2017.05.084**.

23 Z. Ge, F. Ye, H. Cao, G. Leng, Y. Qin and Y. Ding, Carbonate-Salt-Based Composite Materials for Medium- and High-Temperature Thermal Energy Storage, *Particuology*, 2014, **15**, 77–81, DOI: **10.1016/j.partic.2013.09.002**.

24 T. Qian, J. Li, X. Min, Y. Deng, W. Guan and L. Ning, Diatomite: A Promising Natural Candidate as Carrier Material for Low, Middle and High Temperature Phase Change Material, *Energy Convers. Manage.*, 2015, **98**, 34–45, DOI: **10.1016/j.enconman.2015.03.071**.

25 F. Jiang, Z. Ge, X. Ling, D. Cang, L. Zhang and Y. Ding, Improved Thermophysical Properties of Shape-Stabilized NaNO$_3$ Using a Modified Diatomite-Based Porous Ceramic for Solar Thermal Energy Storage, *Renewable Energy*, 2021, **179**, 327–338, DOI: **10.1016/j.renene.2021.07.023**.

26 R. Li, J. Zhu, W. Zhou, X. Cheng and Y. Li, Thermal Properties of Sodium Nitrate-Expanded Vermiculite Form-Stable Composite Phase Change Materials, *Mater. Des.*, 2016, **104**, 190–196, DOI: **10.1016/j.matdes.2016.05.039**.

27 Z. Ge, F. Ye and Y. Ding, Composite Materials for Thermal Energy Storage: Enhancing Performance through Microstructures, *ChemSusChem*, 2014, **7**(5), 1318–1325, DOI: **10.1002/cssc.201300878**.

28 S. Karaman, A. Karaipekli, A. Sarı and A. Biçer, Polyethylene Glycol (PEG)/Diatomite Composite as a Novel Form-Stable Phase Change Material for Thermal Energy Storage, *Sol. Energy Mater. Sol. Cells*, 2011, **95**(7), 1647–1653, DOI: **10.1016/j.solmat.2011.01.022**.

29 Y. Deng, J. Li, T. Qian, W. Guan and X. Wang, Preparation and Characterization of KNO$_3$/Diatomite Shape-Stabilized Composite Phase Change Material for High Temperature Thermal Energy Storage, *J. Mater. Sci. Technol.*, 2017, **33**(2), 198–203, DOI: **10.1016/j.jmst.2016.02.011**.

30 L. Sang and Y. Xu, Form Stable Binary Chlorides/Expanded Graphite Composite Material with Enhanced Compressive Strength for High Temperature Thermal Storage, *J. Energy Storage*, 2020, **31**, 101611, DOI: **10.1016/j.est.2020.101611**.

31 L. André, S. Abanades and G. Flamant, Screening of Thermochemical Systems Based on Solid-Gas Reversible Reactions for High Temperature Solar Thermal Energy Storage, *Renewable Sustainable Energy Rev.*, 2016, **64**, 703–715, DOI: **10.1016/j.rser.2016.06.043**.

32 T. Block and M. Schmücker, Metal Oxides for Thermochemical Energy Storage: A Comparison of Several Metal Oxide Systems, *Sol. Energy*, 2016, **126**, 195–207, DOI: **10.1016/j.solener.2015.12.032**.

33 X. Han, L. Wang, H. Ling, Z. Ge, X. Lin, X. Dai and H. Chen, Critical Review of Thermochemical Energy Storage Systems Based on Cobalt, Manganese, and Copper Oxides, *Renewable Sustainable Energy Rev.*, 2022, **158**, 112076, DOI: **10.1016/j.rser.2022.112076**.

34 X. Chen, M. Kubota, S. Yamashita and H. Kita, Investigation of Sr-Based Perovskites for Redox-Type Thermochemical Energy Storage Media at Medium-High Temperature, *J. Energy Storage*, 2021, **38**, 102501, DOI: **10.1016/j.est.2021.102501**.

35 N. Gokon, T. Yawata, S. Bellan, T. Kodama and H.-S. Cho, Thermochemical Behavior of Perovskite Oxides Based on La$_x$Sr$_{1-x}$(Mn, Fe, Co)O$_{3-\delta}$ and Ba$_y$Sr$_{1-y}$CoO$_{3-\delta}$ Redox System for Thermochemical Energy Storage at High Temperatures, *Energy*, 2019, **171**, 971–980, DOI: **10.1016/j.energy.2019.01.081**.

36 E. Mastronardo, X. Qian, J. M. Coronado and S. M. Haile, Impact of La Doping on the Thermochemical Heat Storage Properties of CaMnO$_{3-\delta}$, *J. Energy Storage*, 2021, **40**, 102793, DOI: **10.1016/j.est.2021.102793**.

37 F. Jin, C. Xu, H. Yu, X. Xia, F. Ye, X. Li, X. Du and Y. Yang, CaCo$_{0.05}$Mn$_{0.95}$O$_{3-\delta}$: A Promising Perovskite Solid Solution for Solar Thermochemical Energy Storage, *ACS Appl. Mater. Interfaces*, 2021, **13**(3), 3856–3866, DOI: **10.1021/acsami.0c18207**.

38 R. Cai, H. Bektas, X. Wang, K. McClintock, L. Teague, K. Yang and F. Li, Accelerated Perovskite Oxide Development for Thermochemical Energy Storage by a High-Throughput Combinatorial Approach, *Adv. Energy Mater.*, 2023, **13**(18), 2203833, DOI: **10.1002/aenm.202203833**.

39 B. Bulfin, J. Vieten, D. E. Starr, A. Azarpira, C. Zachäus, M. Hävecker, K. Skorupska, M. Schmücker, M. Roeb and C. Sattler, Redox Chemistry of CaMnO$_3$ and Ca$_{0.8}$Sr$_{0.2}$MnO$_3$ Oxygen Storage Perovskites, *J. Mater. Chem. A*, 2017, **5**(17), 7912–7919, DOI: **10.1039/C7TA00822H**.

40 S. M. Babiniec, E. N. Coker, J. E. Miller and A. Ambrosini, Investigation of La Sr1−Co M1−O3− (M = Mn, Fe) Perovskite Materials as Thermochemical Energy Storage Media, *Sol. Energy*, 2015, **118**, 451–459, DOI: **10.1016/j.solener.2015.05.040**.

41 E. Mastronardo, X. Qian, J. M. Coronado and S. M. Haile, The Favourable Thermodynamic Properties of Fe-Doped CaMnO$_3$ for Thermochemical Heat Storage, *J. Mater. Chem. A*, 2020, **8**(17), 8503–8517, DOI: **10.1039/D0TA02031A**.

42 S. M. Babiniec, E. N. Coker, J. E. Miller and A. Ambrosini, Doped Calcium Manganites for Advanced High-Temperature Thermochemical Energy Storage, *Int. J. Energy Res.*, 2016, **40**(2), 280–284, DOI: **10.1002/er.3467**.

This journal is © The Royal Society of Chemistry 2025

J. Mater. Chem. A, 2025, **13**, 20028–20043 | **20041**

43 D. Yilmaz, E. Darwish and H. Leion, Utilization of Promising Calcium Manganite Oxygen Carriers for Potential Thermochemical Energy Storage Application, *Ind. Eng. Chem. Res.*, 2021, **60**(3), 1250–1258, DOI: **10.1021/acs.iecr.0c05182**.

44 L. Imponenti, K. J. Albrecht, R. J. Braun and G. S. Jackson, Measuring Thermochemical Energy Storage Capacity with Redox Cycles of Doped-CaMnO $_3$, *ECS Trans.*, 2016, **72**(7), 11–22, DOI: **10.1149/07207.0011ecst**.

45 L. Imponenti, K. J. Albrecht, J. W. Wands, M. D. Sanders and G. S. Jackson, Thermochemical Energy Storage in Strontium-Doped Calcium Manganites for Concentrating Solar Power Applications, *Sol. Energy*, 2017, **151**, 1–13, DOI: **10.1016/j.solener.2017.05.010**.

46 E. Darwish, M. Mansouri, D. Yilmaz and H. Leion, Effect of Mn and Cu Substitution on the $SrFeO_3$ Perovskite for Potential Thermochemical Energy Storage Applications, *Processes*, 2021, **9**(10), 1817, DOI: **10.3390/pr9101817**.

47 E. J. Popczun, D. N. Tafen, S. Natesakhawat, C. M. Marin, T.-D. Nguyen-Phan, Y. Zhou, D. Alfonso and J. W. Lekse, Temperature Tunability in $Sr_{1-x}Ca_xFeO_{3-\delta}$ for Reversible Oxygen Storage: A Computational and Experimental Study, *J. Mater. Chem. A*, 2020, **8**(5), 2602–2612, DOI: **10.1039/C9TA09307A**.

48 F. Li, R. Cai, L. M. Neal and K. H. Bektas, Oxide-Molten Salt Composites for High-Performance Thermal Energy Storage, *US Pat.*, US20240299911A1, 2024.

49 H. Bektas, R. Cai, L. Brody and F. Li, Structural and Thermodynamic Assessment of Ba and Ba/Mg Substituted $SrFeO_{3-\delta}$ for "Low-Temperature" Chemical Looping Air Separation, *Energy Fuels*, 2024, **38**(12), 11107–11118, DOI: **10.1021/acs.energyfuels.4c00859**.

50 L. Marianowski and H. Maru, Latent Heat Thermal Energy Storaap Systems above 450 C, in *12th Intersociety Energy Conversion Engineering Conference*, 1977, vol. 1, pp. 555–566.

51 W. Phillips and J. Stearns, Advanced Latent Heat of Fusion Thermal Energy Storage for Solar Power Systems, in *20th Intersociety Energy Conversion Engineering Conference*, 1985, vol. 2, pp. 2.384–2.391.

52 A. K. Misra, Fluoride Salts as Phase Change Materials for Thermal Energy Storage in the Temperature Range 1000–1400 K: Thermal Analysis and Heat of Fusion Measurements, *J. Electrochem. Soc.*, 1988, **135**(4), 850–854, DOI: **10.1149/1.2095808**.

53 J. D. Whittenberger and A. K. Misra, Identification of Salt—Alloy Combinations for Thermal Energy Storage Applications in Advanced Solar Dynamic Power Systems, *J. Mater. Eng.*, 1987, **9**(3), 293–302, DOI: **10.1007/BF02834148**.

54 N. Verdiev, E. Iskenderov, P. Arbukhanova and A. Amadziev, ТРЕЧКОМПОНЕНТНАЯ СИСТЕМА Na//F, Cl,Br (English Translation:Three-component system Na/F, Cl, Br. Izvestiya VUZov. Severo-Kavkazskii Region), *Nat. Sci.*, 2006, 56–61.

55 C. W. Bale, E. Bélisle, P. Chartrand, S. A. Decterov, G. Eriksson, A. E. Gheribi, K. Hack, I.-H. Jung, Y.-B. Kang, J. Melançon, A. D. Pelton, S. Petersen, C. Robelin, J. Sangster, P. Spencer and M.-A. V. Ende, FactSage Thermochemical Software and Databases, 2010–2016, *Calphad*, 2016, **54**, 35–53, DOI: **10.1016/j.calphad.2016.05.002**.

56 E. Takayama-Muromachi, A. Navrotsky and S. Yamaoka, Calorimetric Study of High-Pressure Polymorphs of Li_2WO_4 and Li_2MoO_4, *J. Solid State Chem.*, 1986, **65**(2), 241–250, DOI: **10.1016/0022-4596(86)90059-9**.

57 S. E. Gustafsson, Transient Plane Source Techniques for Thermal Conductivity and Thermal Diffusivity Measurements of Solid Materials, *Rev. Sci. Instrum.*, 1991, **62**(3), 797–804, DOI: **10.1063/1.1142087**.

58 M. Gustavsson, E. Karawacki and S. E. Gustafsson, Thermal Conductivity, Thermal Diffusivity, and Specific Heat of Thin Samples from Transient Measurements with Hot Disk Sensors, *Rev. Sci. Instrum.*, 1994, **65**(12), 3856–3859, DOI: **10.1063/1.1145178**.

59 Y. He, Rapid Thermal Conductivity Measurement with a Hot Disk Sensor, *Thermochim. Acta*, 2005, **436**(1–2), 122–129, DOI: **10.1016/j.tca.2005.06.026**.

60 A. Jain, S. P. Ong, G. Hautier, W. Chen, W. D. Richards, S. Dacek, S. Cholia, D. Gunter, D. Skinner, G. Ceder and K. A. Persson, Commentary: The Materials Project: A Materials Genome Approach to Accelerating Materials Innovation, *APL Mater.*, 2013, **1**(1), 011002, DOI: **10.1063/1.4812323**.

61 R. Jacobs, T. Mayeshiba, J. Booske and D. Morgan, Material Discovery and Design Principles for Stable, High Activity Perovskite Cathodes for Solid Oxide Fuel Cells, *Adv. Energy Mater.*, 2018, **8**(11), 1702708, DOI: **10.1002/aenm.201702708**.

62 M. Chase Jr. *NIST-JANAF Themochemical Tables*, American Chemical Society, Washington DC, 4th edn, 1998, vol. 9.

63 J. Lopez, G. Caceres, E. Palomo Del Barrio and W. Jomaa, Confined Melting in Deformable Porous Media: A First Attempt to Explain the Graphite/Salt Composites Behaviour, *Int. J. Heat Mass Transfer*, 2010, **53**(5–6), 1195–1207, DOI: **10.1016/j.ijheatmasstransfer.2009.10.025**.

64 A. Anagnostopoulos, M. E. Navarro, M. Stefanidou, Y. Ding and G. Gaidajis, Red Mud-Molten Salt Composites for Medium-High Temperature Thermal Energy Storage and Waste Heat Recovery Applications, *J. Hazard. Mater.*, 2021, **413**, 125407, DOI: **10.1016/j.jhazmat.2021.125407**.

65 R.-A. Mitran, D. Lincu, L. Buhălțeanu, D. Berger and C. Matei, Shape-Stabilized Phase Change Materials Using Molten $NaNO_3$ – KNO_3 Eutectic and Mesoporous Silica Matrices, *Sol. Energy Mater. Sol. Cells*, 2020, **215**, 110644, DOI: **10.1016/j.solmat.2020.110644**.

66 Q. Guo and T. Wang, Study on Preparation and Thermal Properties of Sodium Nitrate/Silica Composite as Shape-Stabilized Phase Change Material, *Thermochim. Acta*, 2015, **613**, 66–70, DOI: **10.1016/j.tca.2015.05.023**.

67 E. Mastronardo, X. Qian, J. M. Coronado and S. M. Haile, Impact of La Doping on the Thermochemical Heat Storage Properties of $CaMnO_{3-\delta}$, *J. Energy Storage*, 2021, **40**, 102793, DOI: **10.1016/j.est.2021.102793**.

68 H. E. Bush, R. Datta and P. G. Loutzenhiser, Aluminum-Doped Strontium Ferrites for a Two-Step Solar Thermochemical Air Separation Cycle: Thermodynamic

20042 | *J. Mater. Chem. A*, 2025, **13**, 20028–20043

This journal is © The Royal Society of Chemistry 2025

Characterization and Cycle Analysis, *Sol. Energy*, 2019, **188**, 775–786, DOI: **10.1016/j.solener.2019.06.059**.

69 W. Pan, S. R. Phillpot, C. Wan, A. Chernatynskiy and Z. Qu, Low Thermal Conductivity Oxides, *MRS Bull.*, 2012, **37**(10), 917–922, DOI: **10.1557/mrs.2012.234**.

70 Y. Liu, K. Chu, Y. Zhou, Y. Li, W. Li and B. Liu, Discovery of Orthorhombic Perovskite Oxides with Low Thermal Conductivity by First-Principles Calculations, *J. Adv. Ceram.*, 2022, **11**(10), 1596–1603, DOI: **10.1007/s40145-022-0632-0**.

71 K. Takahashi, T. Nouchi, M. Sato and T. Ariyama, Perspective on Progressive Development of Oxygen Blast Furnace for Energy Saving, *ISIJ Int.*, 2015, **55**(9), 1866–1875, DOI: **10.2355/isijinternational.ISIJINT-2015-196**.

72 M. Kirschen, H. Pfeifer, F. J. Wahlers and H. Mees, Off-Gas Measurements for Mass and Energy Balances of Stainless Steel EAF, in *Electric Furnace Conference*, 2001, vol. 59, pp. 737–748.

73 S. Yusuf, L. Neal, Z. Bao, Z. Wu and F. Li, Effects of Sodium and Tungsten Promoters on Mg_6MnO_8-Based Core–Shell Redox Catalysts for Chemical Looping—Oxidative Dehydrogenation of Ethane, *ACS Catal.*, 2019, **9**(4), 3174–3186, DOI: **10.1021/acscatal.9b00164**.

74 Q. Yu, Z. Jiang, L. Cong, T. Lu, B. Suleiman, G. Leng, Z. Wu, Y. Ding and Y. Li, A Novel Low-Temperature Fabrication Approach of Composite Phase Change Materials for High Temperature Thermal Energy Storage, *Appl. Energy*, 2019, **237**, 367–377, DOI: **10.1016/j.apenergy.2018.12.072**.

This journal is © The Royal Society of Chemistry 2025

J. Mater. Chem. A, 2025, **13**, 20028–20043 | **20043**